PHYSICAL REVIEW MATERIALS **5**, 114603 (2021)

Primary radiation damage in silicon from the viewpoint of a machine learning interatomic potential

A. Hamedani,[1,*] J. Byggmästar,[2] F. Djurabekova,[2] G. Alahyarizadeh,[1,†]
R. Ghaderi,[1] A. Minuchehr,[1] and K. Nordlund[2]
[1]*Engineering Department, Shahid Beheshti University, G.C, P.O. Box 1983969411,Tehran, Iran*
[2]*Helsinki Institute of Physics and Department of Physics, University of Helsinki, P. O. Box 43, Helsinki FIN-00014, Finland*

(Received 18 August 2021; accepted 25 October 2021; published 5 November 2021)

Characterization of the primary damage is the starting point in describing and predicting the irradiation-induced damage in materials. So far, primary damage has been described by traditional interatomic potentials in molecular dynamics simulations. Here, we employ a Gaussian approximation machine-learning potential (GAP) to study the primary damage in silicon with close to *ab initio* precision level. We report detailed analysis of cascade simulations derived from our modified Si GAP, which has already shown its reliability for simulating radiation damage in silicon. Major differences in the picture of primary damage predicted by machine-learning potential compared to classical potentials are atomic mixing, defect state at the heat spike phase, defect clustering, and recrystallization rate. Atomic mixing is higher in the GAP description by a factor of two. GAP shows considerably higher number of coordination defects at the heat spike phase and the number of displaced atoms is noticeably greater in GAP. Surviving defects are dominantly isolated defects and small clusters, rather than large clusters, in GAP's prediction. The pattern by which the cascades are evolving is also different in GAP, having more expanded form compared to the locally compact form with classical potentials. Moreover, recovery of the generated defects at the heat spike phase take places with higher efficiency in GAP. We also provide the attributes of the new defect cluster that we had introduced in our previous study. A cluster of four defects, in which a central vacancy is surrounded by three split interstitials, where the surrounding atoms are all 4-folded bonded. The cluster shows higher occurrence in simulations with the GAP potential. The formation energy of the defect is 5.57 eV and it remains stable up to 700 K, at least for 30 ps. The Arrhenius equation predicts the lifetime of the cluster to be 0.0725 μs at room temperature.

DOI: 10.1103/PhysRevMaterials.5.114603

I. INTRODUCTION

From the very early efforts to characterize the interaction of energetic particles with matter [1–4] until now when purposeful irradiation of materials has become vital in several applications [5,6], the study and identification of the modification induced in the structure of irradiated materials has been an ongoing endeavor. The ability of describing or predicting the macro-scale effects of the irradiation on the material, to a great extent, hinges on understanding the early-stage damage caused by collision cascades, known as "primary damage" [7,8]. The fact that our understanding of the effects of particle irradiation on materials has taken its shape progressively over the years is partially due to the inherent nature of the atomic collision cascades; that this process is extremely fast and far from equilibrium [9,10]. This feature makes the observational examination of primary damage at the time scale it forms nearly impossible and leaves the burden of its description on the other methods, computer simulations being the most promising method during the past decades [11].

In an *ideal* world, among the simulation methods, density functional theory (DFT) calculations could provide a realistic picture of the primary damage and evolution of collision cascades. However, the current computational framework of the DFT approach makes this method inapplicable to the large scale problems, from which a near-to-reality, explanatory, extendable, or predictive models of defect generation can be extracted. As a result, molecular dynamics (MD) simulations based on analytical potentials, through which significantly larger time- and length-scales (compared to the DFT) is reachable, have become the main line to follow in the simulation of primary damage in materials [11–14]. The reliability of the description that the MD method provides depends almost completely on the quality of the interatomic potential. Traditional potentials are fast and scale linearly with the number of atoms in the system. Their speed comes from the relatively simple mathematical function that is based on a physical understanding of interatomic bonding in the material [15–19]. The function has a handful of global fitting parameters. Once optimized, these parameters are fixed and used for predicting the energy and forces of the new configurations in the simulation. Considering that the true interactions in metallic and covalent systems are determined by complex mechanical many body electronic interactions, it is clear that a unique, mathematically simple function with a number of fixed parameters cannot represent all of the underlying physical and

---

[*] Corresponding author: a_hamedani@sbu.ac.ir; ali.hamedani.fme@gmail.com

[†] Corresponding author: g_alahyarizadeh@sbu.ac.ir

chemical aspects of the system, describes why the accuracy that is reachable by classical interatomic potentials is inherently limited.

In the newer class of interatomic potentials, machine learning (ML) potentials, the generality or higher flexibility lies in the scheme that they are generated. Instead of targeting a particular set of properties to be reproduced, the configurational space of the system (which for a system of N atoms is $3N$-dimensional) is sampled in order to reproduce or "learn" the potential energy surface (PES) of the system [20,21]. Sampling points are DFT-generated energies and forces of a range of configurations, collected in the data set. Learning is achieved via numerical algorithms, in which a large number of tunable parameters are involved. These parameters are optimized in the training process, so that a smooth PES is mapped. The energies of the newly encountered configurations in the simulation is then calculated by interpolating between the reference energies on the constructed PES.

Gaussian approximation potential (GAP) [20] is a class of ML potentials that uses Gaussian process regression in the learning (regression) stage. The idea behind reproducing the PES by ML potentials can be introduced by starting from the following representation [22]:

$$E = \sum_{i} E_i, \tag{1}$$

in which the total energy of the system E is defined as a summation over contributions of individual atoms in the system E_i. E_i is acquired in a two-step process. First, the local environment of the atom i is encoded into a set of structural parameters $\hat{\mathbf{h}}_i$. The encoding of the atomic environments is done by a structural descriptor [23–26] that should be rotationally, translationally, and permutationally invariant. The description provided by the descriptor is based on the positional vectors of the neighbor atoms within the cutoff sphere. Moreover, in multielemental systems, the chemical diversity of the atoms is also considered by the descriptor [27,28]. In the second step, the implemented regression model maps the local atomic environment around atom i on the E_i. The outcome of the summing E_i over all atoms in the system would be the total energy, which is a representative point on the PES of the system. For the first step, GAP uses the SOAP [23] structural descriptor, and takes advantage of Gaussian process regression in the second step. The Eq. (1) can then be rewritten in the form of

$$E_{\mathrm{GAP}} = \sum_{i}^{N} \epsilon(\hat{\mathbf{h}}_i) \tag{2}$$

Although E_{GAP} has a many-body character, it is also possible to append an external potential to it. This could be used with the purpose of either handling a specific range of configurations with the desired part of the potential (e.g., with the external potential), or just to strengthen the overall energy calculation by the addition of an external and fixed n-body potential. In our case, the GAP has been equipped with a pair potential V_{pair} that is meant to deal with the extreme repulsion of atoms in the collision cascades. The energy of the system is then represented by

$$E_{\mathrm{tot}} = \sum_{i<j}^{N} V_{\mathrm{pair}}(r_{ij}) + E_{\mathrm{GAP}}. \tag{3}$$

A successfully trained machine-learning potential inherits the same DFT level-of-accuracy of the data set upon which has been built. On the other hand, the fact that the ML potentials calculate the energies and forces by interpolating the training data makes the them significantly faster than DFT calculations (yet noticeably slower that classical potentials) [29]. Hence, the simulation capability that has been made available by ML potentials makes larger scale molecular dynamics simulations with DFT accuracy reachable [30–39]. That is why they have received a great amount of interest in the community and their implementation in different fields matures rapidly [40–44].

As an element that has been extensively studied due to its key role in the semiconductor industry, there are many classical interatomic potentials for silicon [18,45–48]. So far, radiation damage and defect generation in silicon has been explored using these potentials, with Stillinger-Weber (SW) [18] and Tersoff (T3) [48] potentials being the dominant ones. Recently, a ML potential has been developed for silicon [49]. This potential has the DFT quality of its associated data set, and hence the level of accuracy that is far beyond the reach of any classical interatomic potential. This potential and modifications of it have helped to elucidate some of the key questions about the physical aspects of silicon [34,35,50]. We have recently taken advantage of this GAP potential to carry out large-scale simulations of primary damage in silicon with quantum mechanics precision level. In Ref. [51], we presented our modification of the Si GAP; the modification that aims at the enhancement of GAP‘s performance in the simulation of collision cascades. In Ref. [51], we showed the reliability of the modified GAP compared to experiments by validating the GAP-predicted threshold displacement energies (TDE) in principal directions, the sputtering yields in Ar implantation simulations, and the size of the experimentally detectable irradiation-induced defect clusters. We then simulated cascades initiated by 0.1, 0.2, 0.4, 1.0, and 2.0 keV primary knock-on atom (PKA) energies, and performed similar simulations with the SW and T3 classical potentials. In this work, we present the results of a detailed analysis of the features of the cascade evolution and defect generation in the simulations with GAP. We highlight the differences and similarities between the picture of primary damage that is drawn by the machine-learning and traditional potentials. For that, we explore different aspects of the defect generation at the heat spike phase, and the final state of the resultant damage. We also investigate the structure and the energetics of the defect cluster that we observed in Ref. [51]. The paper is organized as follows. In Sec. II we present the details of our modification of the original GAP. In Sec. III we discuss the performance of the modified GAP. The analysis of the cascade simulations are outlined in Sec. IV, and conclusions are presented in Sec. V.

II. REPULSIVE POTENTIAL

When irradiated by energetic particles, cascades of collisions are initiated by the recoiling PKA in the material. Atoms that are involved in the cascades come close together, interacting at distances much shorter than those in the equilibrium state. Hence, depending on the energy, the colliding dimer can reach potential energies well above the energy corresponding to the ground state of the crystal. Since the original GAP has been trained to the equilibrium properties, the high potential energy of colliding atoms will be underestimated. To capture the repulsion of the colliding atoms in cascade simulations, we carried out a modification of the original GAP [51]. In Ref. [51], we demonstrated the results obtained by implementing the modified GAP and the modification itself was just briefly introduced. In this section we provide the details of this modification; that is a smooth joining of the all-electron DFT repulsive potential, DMol [52], to the original potential. The original and modified GAP potential have been referred to as org-GAP and mod-GAP in the subsequent sections, respectively.

The DMol-DFT data [52] is obtained from exclusively optimised calculations for the high-energy repulsive interactions and its excellent agreement with the experiments has been verified [53]. The V_{pair} potential represents the DMol-DFT repulsive potential in the mod-GAP, that is responsible to take care of the configurations in which the atomic distances are much shorter than the equilibrium distances (collisions). Since the org-GAP has been trained over equilibrium and near-equilibrium states, the short-distance configurations are not present in its training data set. Hence, there is no overlap between the configurations that are covered by the V_{pair} and the org-GAP. Thus, the augmentation of the V_{pair} can be done without re-training the org-GAP, and V_{pair} was appended to the org-GAP. Since any interference with the original reference structures in the data set will affect the equilibrium behavior of the potential, we first found the minimum interatomic distance present in the training data set $d_{\text{smin}} = 1.6$ Å, that becomes the joining point of the V_{pair} and the org-GAP. The V_{pair} is a cubic spline fit to the DMol Si-Si data, through which we could control the smoothness at the joining point (quality of the joining). The smoothness of the joining at d_{smin} was rigorously checked during the augmentation. This was done by monitoring the potential energy and forces on the atoms in a Si-Si dimer that are obtained by the resultant mod-GAP, to make sure that the potential energy and its derivative are continuous at the joining. Any non-smooth turn or variation in the potential energy will be appeared as a kink in the force plot. Joining the DMol data, as it is, to the org-GAP led to a relatively non-smooth transition between the org-GAP and the V_{pair} (top and middle panels in Fig. 1), which was resolved by an average shift of about 2 eV in the V_{pair} over the range of $[1.1 - d_{\text{smin}}]$Å (the smooth V_{pair} in bottom panel in Fig. 1). The V_{pair} then mathes the DMol at 1.0 Å. The fit was then updated and V_{pair} was added to the org-GAP in a tabular format. Figure 2 compares the repulsive interaction of a Si-Si dimer calculated by mod-GAP and DFT with the DMol-DFT data.

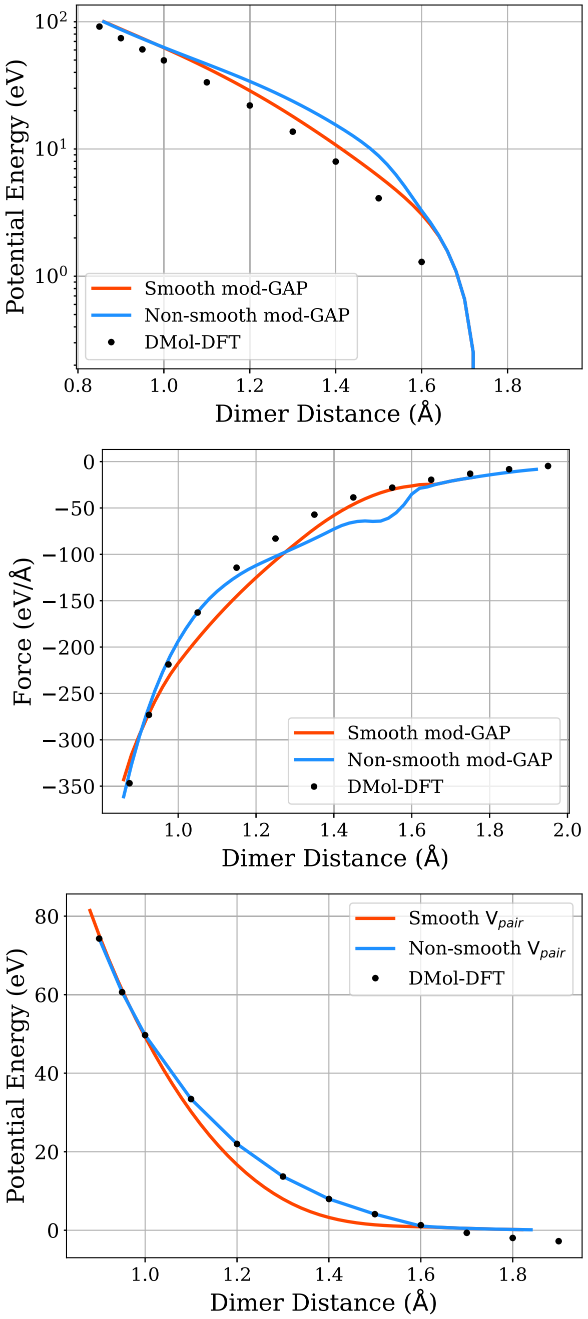

FIG. 1. Distance-wise difference in the potential energy (top) and forces (middle) of a Si-Si dimer with respect to the equilibrium. The top and middle plots are derived form the MD simulations using ”Smooth” and ”Non-smooth” mod-GAP potentials. The ”non-smooth mod-GAP” represents joining the DMol repulsive data, as it is, in the form of the V_{pair} cubic spline fit to the org-GAP potential. The joining point is $d_{\text{smin}} = 1.6$ Å. The non-smooth mod-GAP yields a relatively sharp transition to the V_{pair}. This problem was resolved by re-fitting the V_{pair} to the DMol data in which the potential energies in the distance range starting from d_{smin} to the 1.1 Å have an average downward shift of approximately 2 eV (the smooth V_{pair}, bottom). The V_{pair} then matches the DMol at 1.0 Å. The resultant smooth mod-GAP potential was used to carry out the simulations in the paper.

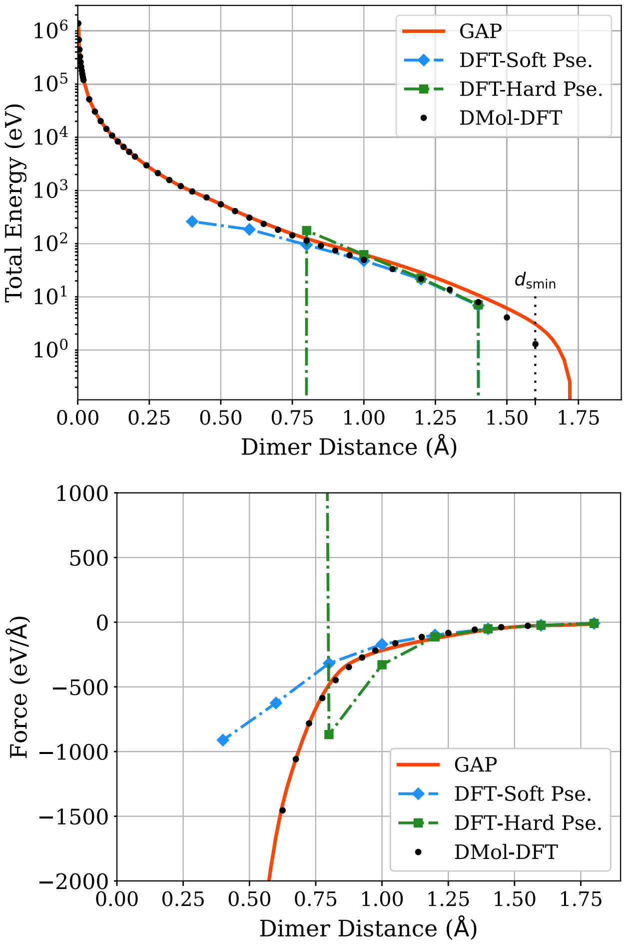

FIG. 2. Total energy (top) and exerted force (bottom) of a repulsing Si-Si dimer, as a function of distance. Simulation setup is made up of two silicon atoms within a $(3 \times 3 \times 3)a_0$ cell, $a_0 = 5.461$ being the lattice constant with, that one moves toward the other one with the step size of 0.2 Å. GAP represents our modified GAP potential, which is the original GAP joined to the DMol repulsive potential at $d_{\mathrm{smin}} = 1.6$ Å. Comparison is made with the results from GGA DFT simulations with two PAW potentials; the soft one has 4 valence electrons and the harder one has 12 valence electrons. Sudden jump (drop) in the force (energy) plot is an indication of the attraction between Si atoms. Both the hard and soft pseudopotentials predict an attractive interaction in the distance range of $d > 1.6$ Å. The hard potential shows an abnormal, attractive response in the distance ranges of $d < 0.74$ Å.

DFT calculations were performed with VASP [54–57] package, using the PBE GGA [58] exchange-correlation functional, and projector-augmented-wave (PAW) method [59,60] for the description of the electron-ion interaction. We employed two PAW potentials in this analysis; the hard potential with 12 $2s^2 2p^6 3s^2 3p^2$ valence electrons and the softer one that treats 4 $3s^2 3p^2$ electrons in the valence shell. The default cutoff energies of 547 and 245 eV were used, and a single Γ-point sampling of the Brillouin was carried out. For each PAW potential, reducing the dimer distance continued until the calculation crashed. While the soft potential follows DMol up to 1 Å, the hard potential starts diverging from the soft and from DMol at 1.2 Å. For distances in the range of $d < 0.74$ Å, with an abnormal behavior, the hard PAW potential becomes attractive, showing a jump in the exerted force. Figure 3 compares the repulsive part of the SW, T3, org-GAP, and the mod-GAP potentials along with the DMol data. As seen, the org-GAP potential does not capture the atomic repulsion. The T3 potential has a very similar profile to the DMol potential and the mod-GAP. The SW potential shows higher energies and a steeper gradient than the mod-GAP and T3 potentials in the range of $d < 1.25$ Å. The higher repulsive energy of the SW potential can justify its higher prediction of the threshold displacement energies in principal directions with respect to the mod-GAP and T3 potentials [49].

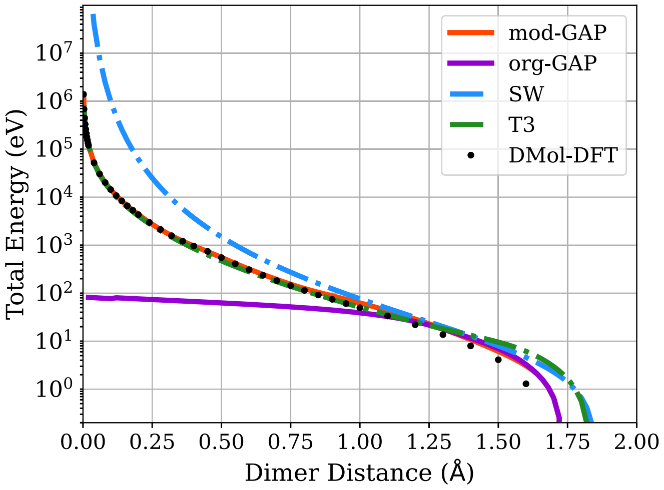

FIG. 3. The repulsive part of the SW, T3, org-GAP, and mod-GAP potentials.

III. PERFORMANCE OF THE MODIFIED POTENTIAL

A. Equilibrium state

The equilibrium part of the potential is responsible for the post-heat-spike phase in the cascades where the hot liquid-like region generated in the heat-spike cools down and the defect structures are formed. In order to make sure that our augmentation has not affected the primary training data set of the potential (that represent the equilibrium/near-equilibrium states), in Ref. [51] we calculated thermal and mechanical properties using the mod-GAP and made a comparison between the prediction of the org-GAP and mod-GAP. Calculated properties include elastic constants, bulk modulus, melting temperature, and radial distribution function of liquid and amorphous phases. The results that are reported in [51] show that the predictions of the two potentials are equal within the error bars, confirming that the equilibrium part of the potential has remained intact.

B. Quasi-static simulations

To further asses the performance of the mod GAP in cascade simulations, we here conducted three tests, first one being quasistatic drag calculations [61–63]. In these calculations, an atom is moved in a certain direction, along which it encounters short-range interactions as a result of passing through very close neighborhood of some of the other

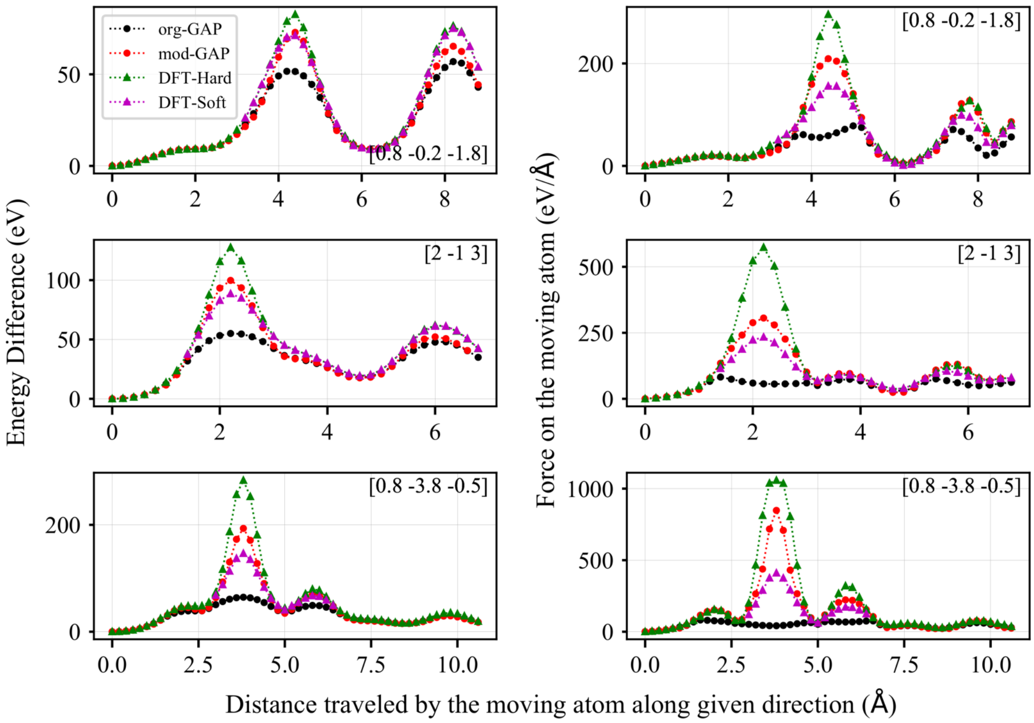

FIG. 4. Quasistatic drag in three representative directions in silicon.

atoms in the system. The short-range interaction is seen as a peak in the step-wise energy-difference monitoring of the moving atom. The simulation setup includes a 64-atom box ($2 \times 2 \times 2$) in which the moving atom travels along a given direction with the step size of 0.3 Å. DFT calculations were performed with the same settings that were introduced in Sec. II.

Figure 4 provides the results of the simulations in three representative directions, where the predictions of mod-GAP, org-GAP, and DFT calculations have been compared. As seen, the org-GAP does not capture the higher energy in short-range interactions of the moving atom, whereas the mod-GAP reflects the energy difference as the interatomic distance gets smaller. The repulsive response of the mod-GAP is closer to the DFT results obtained by the soft PAW potential than to that estimated by the hard potential. However, since the all-electron DMol repulsive potential, that mod-GAP takes the advantage of, has been exclusively developed for extremely short-range (down to 0.001 Å) interactions, we believe that the mod-GAP's profile is more reliable in portraying repulsive energy landscape. Regarding the behavior of the PAW potentials in the interactions in the range of $d < 1.0$ Å, we believe that the soft potential is more reliable. This is due to the unphysical behavior of the hard potential in the range of $d < 0.74$ Å observed in Sec. II.

C. TDE calculations

The threshold displacement energy is one of the fundamental parameters in characterizing the early-stage defect generation and radiation resistance of the materials [7]. In Ref. [51] we calculated the TDE values in principal directions with mod-GAP where we found excellent agreement between the prediction of GAP and DFT and experimental values. Here, we simulate the complete symmetry-reduced directional TDE surface at 30 K by mod-GAP.

The simulations were performed based on the method outlined in [64]. A simulation box containing 4096 atoms ($8 \times 8 \times 8$ unit cells) was used. To check the box size, a few simulations in some random directions with PKA energies up to 62 eV were initially carried out and in none of the cases the PKA atom reached to the border of the box. This assured us of the box size being large enough. Around 140 directions were considered in the calculations, among which nearly 50 directions represent uniform-sampling and 90 directions correspond to the sampling by a constant 5° interval. The method introduced in [65] was implemented for uniform sampling of the directions. Moreover, to enrich the sampling, additional simulations were also carried out where needed. A 4 eV kinetic-energy increment was used in the search for the defect generation by the PKA atom. The global average TDE, integrated over all directions was calculated by [64]

$$T_{\text{ave}} = \frac{\iint T(\theta, \varphi) \sin\theta d\theta d\varphi}{\iint \sin\theta d\theta d\varphi} \tag{4}$$

where $T(\theta, \varphi)$ is the TDE value for the given (θ, φ) direction. The T_{ave} values by mod-GAP, SW, and T3 potentials are 22 ± 0.82, 32.87 ± 0.90, and 20.45 ± 0.42 eV, respectively. The global minimum by GAP, SW, and T3 is 10 ± 0.5, 18 ± 0.5, and 10 ± 0.5 eV, respectively. For the T3 potential the global minimum is found in the [100] direction. For the SW potential the global minimum is seen in ($\theta = 45^\circ, \varphi = 15^\circ$) direction, and the second smallest TDE value (20 ± 0.5 eV) is found in [111] direction. However, with the GAP potential the global minimum does not occur in any of the low-index directions.

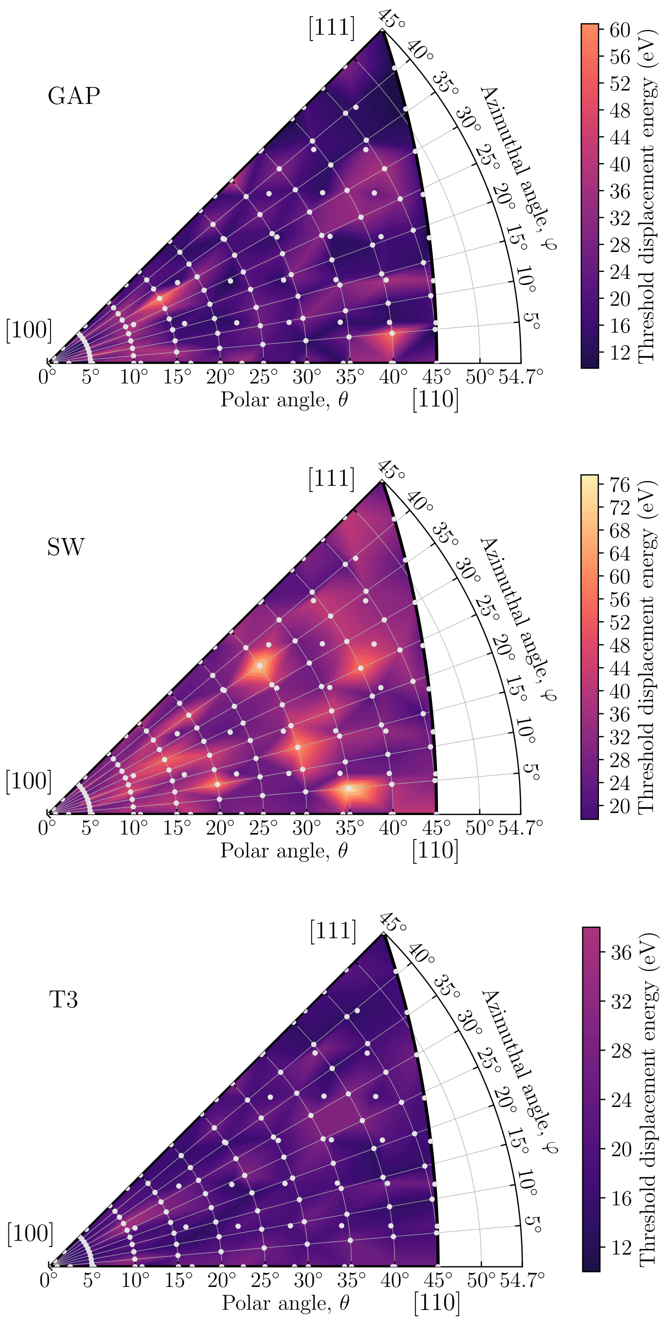

FIG. 5. Threshold displacement energies calculated by mod-GAP, SW, and T3 potentials at 30 K. The global averages are 19.63, 30.63, and 20.17 eV for mod-GAP, SW, and T3, respectively. The global minimum by GAP, SW, and T3 is 10 ± 0.5, 20 ± 0.5, and 10 ± 0.5 eV, respectively. The [111] direction in the maps corresponds to the nearest-neighbour collision path of the atoms in ⟨111⟩ directions.

Figure 5 presents the TDE surfaces obtained by three potentials. The difference between the predictions of the potentials and the higher minimum value by SW is visible. Since mod-GAP has already shown [51] a perfect agreement with the DFT values in low-index directions, a realistic estimation in the other directions can also be expected although reporting the directional TDE values from simulations must be done carefully. This is due the fact that the anisotropic nature of the TDE surface and thermal vibrations of the atoms could cause a considerable difference between the TDE values in exactly [hkl] direction and a direction that locates just a few degrees away form it (a smeared-out threshold for the given direction versus a sharp one). Further discussion on this topic can be found in [62–64,66].

The output of the TDE simulations in cases that the stable defect has been generated is a Frenkel pair. Among all tested energies in our trial in low-index directions, we selected those simulations with mod-GAP, which led to the defect generation, and analyzed the type of the interstitials that were created. We observed ⟨110⟩-split, tetrahedral, and hexagonal interstitials with the occurrence of 46%, 29%, and 25%, respectively. Regarding the formation energy of these defects, GAP shows excellent agreement with the DFT [49], hence a realistic, DFT-accurate prediction can be expected. We confirm that there is no dependence between the type of the interstitial and the energy or the direction of the PKA in GAP's prediction, as we found all types of interstitials in each of the crystal directions with different PKA energies. The performance of the GAP becomes more interesting when the same analysis is performed for the SW and T3 potentials as well. In the SW and T3 simulations, we found no hexagonal interstitials, only ⟨110⟩-split and tetrahedral interstitials. ⟨110⟩-split was the dominant type in SW simulations and tetrahedral in T3 simulations. The summary of the analysis for potentials along with the relative error of their predicted formation energy (FE) with respect to the DFT is presented in Table I. The ratio of the occurrence of each interstitial type in the simulations with classical potentials can be linked to the relative formation energies of the different interstitial configurations. For example, with the T3 potential, the tetrahedral interstitial is the stable one and its occurrence is higher than ⟨110⟩-split. However, GAP predicts the ⟨110⟩-split to be the stable interstitial, as has already been confirmed by *ab initio* calculations [67], and provides a balanced distribution between the interstitial types.

IV. CASCADE SIMULATIONS

The cascade simulations on which we carry out our analysis are the same simulations that we conducted in Ref. [51]. Here, we carry out further and more detailed analysis to cover different aspects of the defect generation in collision cascades, and compare the results produced by mod-GAP, SW, and T3 potentials, indicating the differences between their predictions.

A. Simulation Details

All cascade simulations were carried out with LAMMPS [68,69] compiled with QUIP [70] to support the GAP. Simulations were performed for 0.1, 0.2, 0.4, 1.0, and 2.0 keV PKA energies at 300 K. The size of the simulation box depends on the recoil energy, such that it contains 40–46 atoms for every electron volt of the PKA energy (e.g., 8000 atoms for 0.2 keV PKA simulations). Periodic boundary conditions were applied in all directions. After minimization of the box using the conjugate gradient (CG) algorithm, initial random velocities were assigned to the atoms to simulate a temperature of 300 K. The

TABLE I. Occurrence (%) of the ⟨110⟩-split, tetrahedral, and hexagonal interstitials in our TDE simulations with GAP, T3, and SW potentials. Relative error (%) of the formation energy (FE) of each interstitial type, compared to the DFT, has been taken from [49].

	⟨110⟩-split		Tetrahedral		Hexagonal	
Pot.	Occ.	FE err.	Occ.	FE err.	Occ.	FE err.
GAP	46	−2	29	−7	25	−3
SW	67	22	33	28	0	77
T3	27	32	73	−7	0	27

entire cell was then equilibrated at 300 K with the canonical *NVT* ensemble for 30 ps. After that, the box was further relaxed with the isothermal-isobaric *NPT* ensemble at 300 K and zero pressure for another 30 ps. Finally, with an increased damping parameter, the lattice was relaxed for another 30 ps at 300 K and zero pressure. At all stages, the time step was 1 fs. The cascades were initiated by giving a kinetic energy to a PKA atom at the center of the box along a randomly-selected direction. For each energy, 20 simulations were performed. The temperature along the borders of the simulation cell was controlled by applying a Langevin thermostat [71]. This enables dissipation of excess heat introduced by PKA to the bulk of material and dampens pressure waves created at the core of the cascades. Electronic stopping [72] was applied as a nonlocal friction force to the atoms with kinetic energies above 10 eV. The adaptive time step algorithm [73] was used to integrate the equations of motion. The simulation time was 6 ps, after which the entire cell had cooled down to 300 K.

B. Defect generation

Table II summarizes the results associated with the defect generation and cascade dynamics for the three potentials. This includes the PKA energy E, the damage energy E_{dam} defined as the portion of the PKA energy that is deposited to the lattice atoms in collision cascades, the final number of interstitial defects $N_{\text{int}}^{\text{surv}}$ that have survived at $t = 6$ ps where the system has reached equilibrium at 300 K and the number of defects has been saturated, the number of coordination defects (dangling + floating bonds) at the heat spike $N_{\text{coord}}^{\text{spike}}$ and at the equilibrium $N_{\text{coord}}^{\text{surv}}$, the mixing parameter Q, the number of atoms displaced by more than half the nearest-neighbor distance N_{disp}, the number of atoms whose average kinetic energy is above the energy corresponding to the melting point of the material ($\frac{3}{2}kT_{\text{melt}}$) N_{hot}, and the duration of the heat spike phase t_{spike}. E_{dam} was calculated by subtracting the total energy lost to the electronic stopping, E_{els}, from the PKA energy. E_{els} was calculated using the SRIM [74] package. Interstitials and vacancies were identified using Wigner-Seitz cell analysis as implemented in the OVITO package [75]. The coordination defects were obtained with the cut-off radius of $r = 2.75$ Å. The mixing parameter was calculated using the formula [76]

$$Q = \frac{\sum_i |r_{\text{i}}(t) - r_{\text{i}}(0)|^2}{6 n_0 E_{\text{dam}}} \tag{5}$$

where n_0 is the atomic density, and with $r_{\text{i}}(t)$ being the position vector of the atom i at time t, $\sum_i |r_{\text{i}}(t) - r_{\text{i}}(0)|^2$ represents the square of atomic displacements magnitudes at time t, summed over all atoms in the simulation box. The Q and N_{disp} values are reported at $t \approx 2$ ps, which was chosen visually from their time-dependent profiles; the time at which

TABLE II. Number of defects at the heat spike and the final equilibrium state, as well as mixing, number of displaced atoms, number of energetic atoms, and the duration of heat spike. Detailed information about the quantities is provided in the text. $N_{\text{int}}^{\text{surv}}$ was calculated at $t = 6$ ps. Q and N_{disp} were obtained at $t \approx 2$ ps. N_{hot} is reported at the specified time of the heat spike. The results of each case represent the average over 20 simulations. Uncertainties are standard errors.

Potential	E (keV)	E_{dam} (keV)	$N_{\text{int}}^{\text{surv}}$	$N_{\text{coord}}^{\text{spike}}$	$N_{\text{coord}}^{\text{surv}}$	Q (Å^5/eV)	N_{disp}	N_{hot}	t_{spike} (ps)
mod-GAP	0.1	0.08	1 ± 0.1	48 ± 1	10 ± 1	18 ± 1	13 ± 1	57 ± 1	0.39 ± 0.026
	0.2	0.16	2 ± 0.2	83 ± 2	17 ± 2	21 ± 1	29 ± 2	111 ± 2	0.41 ± 0.023
	0.4	0.31	4 ± 0.4	161 ± 3	24 ± 2	24 ± 1	67 ± 3	224 ± 3	0.48 ± 0.023
	1.0	0.75	13 ± 1	343 ± 21	54 ± 3	32 ± 1	187 ± 11	541 ± 11	0.52 ± 0.024
	2.0	1.45	27 ± 4	543 ± 34	102 ± 3	36 ± 1	370 ± 28	980 ± 28	0.57 ± 0.020
SW	0.1	0.08	1 ± 0.1	24 ± 1	6 ± 1	9 ± 0.2	7 ± 0.4	49 ± 1	0.18 ± 0.025
	0.2	0.16	2 ± 0.2	48 ± 1	9 ± 1	11 ± 0.2	17 ± 1	97 ± 2	0.21 ± 0.018
	0.4	0.31	4 ± 0.4	87 ± 2	20 ± 2	14 ± 0.2	41 ± 2	191 ± 2	0.17 ± 0.019
	1.0	0.75	11 ± 1	185 ± 10	47 ± 3	19 ± 1	117 ± 6	477 ± 7	0.22 ± 0.021
	2.0	1.45	27 ± 2	326 ± 12	103 ± 6	20 ± 1	235 ± 14	923 ± 19	0.20 ± 0.010
T3	0.1	0.08	2 ± 0.2	30 ± 1	14 ± 1	10 ± 0.2	7 ± 0.3	27 ± 0.5	0.13 ± 0.017
	0.2	0.16	5 ± 0.3	60 ± 2	29 ± 2	12 ± 0.3	15 ± 1	50 ± 1	0.19 ± 0.017
	0.4	0.31	9 ± 0.4	106 ± 4	52 ± 3	16 ± 1	31 ± 1	100 ± 2	0.21 ± 0.014
	1.0	0.75	22 ± 1	235 ± 11	110 ± 3	19 ± 1	80 ± 4	248 ± 4	0.25 ± 0.026
	2.0	1.45	40 ± 1	363 ± 22	205 ± 5	20 ± 1	154 ± 7	470 ± 14	0.24 ± 0.018

TABLE III. Results of the cluster analysis of the final Wigner-Seitz defects at $t = 6$ ps, obtained from simulations using mod-GAP, SW, T3 potentials. The analysis was performed with the cutoff value of $r_{\text{cl}} = 10.8$ Å. Clusters are identified by the number of contained defects, "isolated" being a single defect. E is the PKA energy in keV and N_{def} is the total number of defects (interstitials+vacancies). For the clusters of size X, f_{occ} is the total frequency of occurrence; F is the total fraction(%) of defects; F_{v} is the fraction (%) of vacancies; F_{i} is the fraction (%) of the interstitials, and $F_{\text{v}}/F_{\text{i}}$ shows the ratio of the fraction of vacancies to interstitials. The results for each case represent the average over 20 simulations. The 0.1, 0.2, and 0.4 keV PKAs do not produce large size clusters.

			Isolated					2–10 def.					10–30 def.					>30 def.				
Pot.	E	N_{def}	f_{occ}	F	F_{v}	F_{i}	$F_{\text{v}}/F_{\text{i}}$	f_{occ}	F	F_{v}	F_{i}	$F_{\text{v}}/F_{\text{i}}$	f_{occ}	F	F_{v}	F_{i}	$F_{\text{v}}/F_{\text{i}}$	f_{occ}	F	F_{v}	F_{i}	$F_{\text{v}}/F_{\text{i}}$
mod-GAP	0.1	2	1.25	59	19	40	0.48	0.45	41	27	14	1.93	0.0					0.0				
	0.2	4	1.85	48	10	38	0.26	0.95	52	39	13	3.0	0.0					0.0				
	0.4	8	2.6	37	4	33	0.12	1.25	53	43	10	4.3	0.1	9	5	4	1.25	0.0				
	1.0	26	5.55	26	2	24	0.08	2.05	36	23	13	1.77	0.45	28	18	10	1.8	0.1	10	6	4	1.5
	2.0	54	9.4	24	3	21	0.14	3.5	33	21	12	1.75	0.35	14	10	4	2.5	0.35	29	16	13	1.23
SW	0.1	2	0.75	38	16	22	0.73	0.60	62	32	30	1.07	0.0					0.0				
	0.2	4	0.75	23	3	20	0.15	0.90	77	47	30	1.57	0.0					0.0				
	0.4	8	0.65	11	4	7	0.57	0.75	50	27	23	1.17	0.4	39	20	19	1.05	0.0				
	1.0	22	1.35	8	1	7	0.14	1.0	23	10	13	0.8	0.7	55	30	25	1.2	0.15	14	8	6	1.33
	2.0	54	2.45	6	1	5	0.20	1.1	12	5	7	0.71	0.8	35	18	17	1.06	0.55	47	25	22	1.14
T3	0.1	4	0.8	35	14	21	0.67	0.70	65	34	31	1.09	0.0					0.0				
	0.2	10	0.6	11	1	10	0.1	0.65	50	28	22	1.27	0.4	39	20	19	1.05	0.0				
	0.4	18	1.1	7	0	7	0.0	0.25	9	5	4	1.25	0.9	82	45	37	1.22	0.0				
	1.0	44	2.0	5	0	5	0.0	0.45	5	2	3	0.67	0.15	12	7	5	1.4	0.85	78	42	36	1.16
	2.0	80	3.0	5	0	5	0.0	0.40	2	0.7	1.3	0.54	0.35	12	7	5	1.4	0.95	81	43	38	1.13

saturation of Q in three potentials and almost in all PKA energies is visible.

The heat spike, the repulsive part, and the melting point of the potential affect the number of displaced atoms and the mixing parameter [76,77]. The higher number of displaced atoms in mod-GAP seen in Table II can be related to its melting point, as it has the lowest melting point among three potentials. Lower melting point leads to a greater number of atoms in the molten zones, or higher N_{hot}. During the cooling-down of the cascades, these hot atoms can recrystallize in new lattice sites, thus being labeled "displaced". Mixing in mod-GAP is greater than SW and T3 potentials by a factor of two, which is in line with the higher number of displaced atoms with GAP. This difference can also be justified from the heat-spike point of view that is entangled with the melting point predicted by the potentials. Besides the fact that there are fewer number of hot atoms in the potential with the higher melting point (hence the overall atomic displacement magnitude is lower), the heat spike in the potential that has higher melting point is shorter (Table II) that reduces the distances, which the hot atoms travel within molten zones.

The repulsive part of the potentials are not fully consistent with the Q values or number of displaced atoms. T3 has very similar repulsive potential to that of mod-GAP (Fig. 2) and hence the number of displaced atoms are expected to be close. However, mod-GAP shows around 1.5 times more displaced atoms. On the contrary, the greater number of displaced atoms in SW with respect to the T3 is consistent with the higher repulsion by SW in $d \leqslant 1.2$ Å. Regarding the interstitials, the SW and mod-GAP potentials show very similar number of surviving defects, whereas T3 potential produces almost two times more defects at all energies. The number of interstitials at the heat spike is also different in potentials [51]; for instance, for the PKA energy of 2 keV, mod-GAP shows higher value (110 ± 9) than SW (78 ± 7) and T3 (66 ± 5) potentials. Recovery of the crystalline phase from the molten region that is generated in the heat spike is also different in the three potentials. Although mod-GAP and SW yield almost identical final number of coordination defects, recovery in mod-GAP takes place from noticeably higher number of defects, but within the same interval as in SW. In other words, recrystallization in GAP has higher rate or efficiency.

C. Cluster analysis

Cluster analysis was carried out by defining a cluster as a set of neighboring Wigner-Seitz defects, neighbors being defects located within a range up to the cutoff value of $r_{\text{cl}} = 2a_0 \approx 10.8$Å [79]. The size of the cluster is specified by the number of defects that are contained within the cluster. We considered the single (isolated) defects and the groups of clusters with the sizes of 2–10, 10–30, and >30 defects in our analysis. The results are compiled in Table III.

In clustering of the final defects, there are two major differences between the mod-GAP and classical potentials. The first difference is that in GAP, defects are more likely to be clustered in smaller packs than in bulky pockets. This feature is visible in the occurrence-frequency and the fraction of defects in the clusters. Averaging over all energies, mod-GAP shows 3 and 4 times more isolated defects compared to SW and T3 potentials, respectively. Considering the energies individually, the difference still exists but the factors are different. Similarly, the defects in the small clusters (2–10 defects) are 1.5 and 6 times more (notice the frequencies as well) in GAP with respect to the SW and T3. The number of defects that are encapsulated within the largest clusters (>30) is also another verification for the observed difference in mod-GAP, as among three potentials GAP has the lowest fraction of defects in this cluster size division.

We also performed cluster analysis taking the vacancies and interstitils separately into account in the simulation boxes. In the prediction of all potentials, the isolated defects are mostly of interstitial type, though the fractions are different. This could raise an expectation that larger clusters would be vacancy-rich, which is confirmed by a closer inspection of the f_{occ} and $F_{\mathrm{v}}/F_{\mathrm{i}}$ quantities for larger clusters (10–30, >30) in Table III. $F_{\mathrm{v}}/F_{\mathrm{i}}$ is the fractional ratio of vacancies and interstitials in each case. Taking the $F_{\mathrm{v}}/F_{\mathrm{i}}$ for the isolated defects into consideration, its value for all potentials and PKA energies is below 1.0, which indicates the domination of isolated interstitials over isolated vacancies. The distribution in the other size bins shows that the number of vacancies are higher than the interstitials in the clusters, since in *almost* all of the larger-size (nonisolated) groups, the $F_{\mathrm{v}}/F_{\mathrm{i}}$ is greater than 1.0. However, it seems that there is no direct relation between the size of the cluster and the fraction of its vacancies and interstitials. The domination of vacancies over interstitials in the clusters applies for all energies in GAP‘s prediction. For T3 and SW the exception is “2–10 defects” group with 1.0 and 2.0 keV PKA energies, which have <1.0 values but, in the larger cluster sizes, again, vacancies are forming major part of the cluster. So, it could be stated that the vacancies are more likely to be clustered than interstitials.

The second difference in clustering of the defects in mod-GAP, which, in a way, describes its first difference, is the different ”evolution pattern” of the cascades in mod-GAP compared to the T3 and SW potentials. If one considers that (sub)cascades are developing within pocket-like volumes in the cell, in classical potentials these pockets are larger and contain the major portion of displaced atoms, which after cooling down results in in localized and denser clusters of final defects. On the contrary, cascades in the GAP spread across a broader spatial range, creating relatively smaller pockets (hence smaller clusters of final defects) and leaving more isolated defects. In other words, more atoms are involved in the distribution of the injected energy by the PKA in the GAP, while the dissipation of energy is concentrated more locally in the classical potentials. This does not imply that there are no larger clusters in mod-GAP simulations, but rather that the frequency of larger clusters is lower in GAP and that their sizes are smaller than their counterparts in T3 and SW. This observation is confirmed by looking at the *fraction* of defect clusters with the size of “>30 defects” in Table III, where this class of clusters include lower fraction of total defects in mod-GAP compared to T3 and SW.

In order to assess the evolution of the cascades and resulting final clusters in the mod-GAP more quantitatively, we carried out another two analyses. First, we selected the largest defect clusters in our 2 keV PKA energy simulations in three potentials (20 simulations for each potential) and assigned a polyhedral surface to each cluster. The process was done using the associated module implemented in the OVITO package. The probing radius was set to 10.8 Å, same as the cutoff value in our cluster analysis, and smoothening level was set to *zero* in order to have the maximum number of defects enclosed by the generated 3D surface. We then calculated the volume of the constructed geometries around the clusters in three potentials. The mod-GAP with the average volume of $(1248 \pm 407)\,\text{Å}^3$ has smaller volume occupied by the final defect clusters in the box, against T3 with $(6233 \pm 656)\,\text{Å}^3$, and SW with $(1948 \pm 330)\,\text{Å}^3$. In the second analysis we calculated the average distance between the initial position of the PKA, and the center of mass of relatively large clusters that contain 30–45 defects. The average distance in GAP is $(38.5 \pm 3.8)\,\text{Å}$, which is greater than the average value of $(24.3 \pm 6.5)\,\text{Å}$ in T3, and $(25.4 \pm 2.3)\,\text{Å}$ with the SW potential, indicating that in GAP, on average, the atoms, which have been energetically affected by the PKA impact, reside farther away from the PKA position.

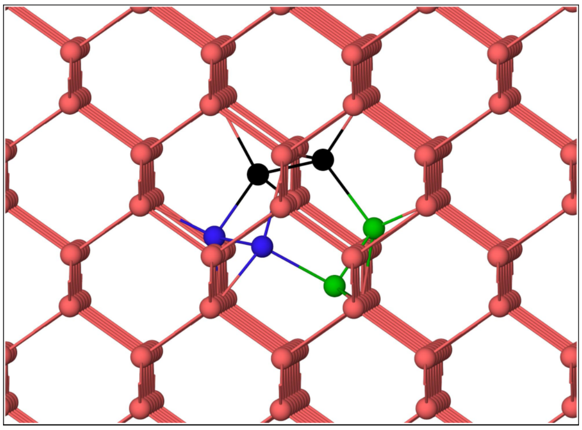

FIG. 6. A defect cluster found in molecular dynamics simulation of collision cascades with the mod-GAP interatomic potential. The cluster is comprised of a central vacancy and three dumbbell interstitials around it. The missing bond in the array of bonds at the center of the image can be helpful in locating the vacant site. Two of the dumbbells that surround the vacancy have [1 0 0] configuration (colored black and blue) and the third dumbbell is a [1 1 0]-type (green). Red atoms show the regular atomic sites in silicon lattice. All of the six atoms around the vacancy are 4-folded. The formation energy of the cluster is 5.57 eV according to DFT.

The presence and structure of the small defect clusters is important when characterizing the performance of semiconductor devices. The optical/electrical activity [80–82], diffusion, interaction, and placement of dopants upon thermal annealing [83–86], and nucleation of extended defects [86,87] can be greatly influenced by the density and configuration of small clusters. In Ref. [51] we observed a new defect cluster in our cascade simulations, which we now analyze and characterize in more detail. The probability of formation of this cluster in the cascades was 0.03, 0.01, and 0 in the simulations by mod-GAP, SW, and T3 potentials, respectively. The cluster is comprised of a central vacancy and three split interstitials that surround the vacancy and is illustrated in Fig 6. In all cases two of the dumbbells are of [1 0 0] type and the third one is a [1 1 0] dumbbell. With one case as exception, the other feature of the cluster is that all of the six atoms that surround the central vacancy are four-folded. The exception is with one of the GAP occurrences where two of the interstitials have a coordination number of three. This feature explains the stability of the cluster upon quenching the system to 0 K. In cases that the surrounding atoms are all four-folded, the defect remains stable without any recombination. However, in the case that the interstitials are three-folded, one of the interstitials combines with the vacancy and the cluster collapses.

To investigate the thermal stability and energetics of this cluster, we checked the stability of the cluster in DFT and in finite-temperature simulations with the mod-GAP. The position of the interstitials and vacancy were extracted (coordination numbers, and relative directional vectors with respect to the surrounding atoms were taken into account) and the cluster was put in a new 512-atom perfect cell, yielding a 514-atom defective cell. The DFT calculations were performed with VASP package as before, with the PBE GGA exchange-correlation functional. The PAW potential with 12 valence electrons was used and the plane-wave cutoff energy was 710 eV was used. Brillouin-zone sampling was performed using Monkhorst-Pack mesh grid of (2 × 2 × 2). To obtain equilibrium geometries, all atoms were relaxed with conjugate gradient method until residual forces on atoms became smaller than 0.01 eV/Å. The cell shape and cell volume were also allowed to change during the relaxation. The defect cluster remained stable during the DFT relaxation. Upon relaxation, the (min,max) displacement among the interstitials is (0.16 Å, 0.30 Å).

We calculated the formation energy of the cluster E_f, defined by $E_f(n) = [E_{\text{tot}}(I_\text{n}) - (1 + n/N)E_{\text{bulk}}(N)]$, where N is the number of atoms in the perfect cell, $E_{\text{tot}}(I_\text{n})$ is the total energy of defected cell with $N + n$ atoms, and E_{bulk} is the total energy of the perfect system. GAP's prediction of E_f is 5.97 eV, while DFT gives a slightly lower value of 5.57 eV. The formation energy of the cluster is comparable to those reported in the previous *ab initio* stability analysis studies of the small defect clusters in silicon. Our 3I+V cluster is an alternative 2I configuration in the net balance of atoms. In Ref. [88] in which the stability and the formation energy of the interstitial clusters, I_n (n $\leqslant$ 10), has been studied, the formation energy of the I_2 cluster was reported to be 5.58 and 5.04 eV with the GGA and LDA calculations, respectively. Also, a value of 5.66 eV with the GGA functional in a 216-atom box has been reported in Ref. [89]. These values are very close to the 5.57 eV by our GGA DFT of the new cluster, indicating that its stability is similar to other clusters of the same size. The experimental E_f value for I_2 cluster can be found in Ref. [78], which amounts to 3.34 eV. In an earlier attempt a value of 2.6 eV had also been reported [89]. These experiments have been performed in high temperature conditions (600–800 C) and the inverse model has been implemented to derive the reported values.

To further investigate thermal activation of the cluster we conducted annealing simulations at the temperature range of (400–1600)K. The cluster remains stable up to 700 K, for at least 30 ps and collapses at 740 K. The cluster collapses into two interstitials, that remain stable up to 50 ps. One of the interstitials is a [1 1 0] dumbbell and the other one is a tetrahedral interstitial. Regarding the transformation path of the cluster, although the final configuration that the cluster collapses into is similar in all cases (a [1 1 0] dumbbell and a tetrahedral interstitial), the atom that becomes the tetrahedral interstitial or the atoms that are building the [1 1 0] dumbbell are not identical. Moreover, the location of the interstitial and the orientation of the dumbbell are also different in simulations. As a result, a unique recombination path is not achieved.

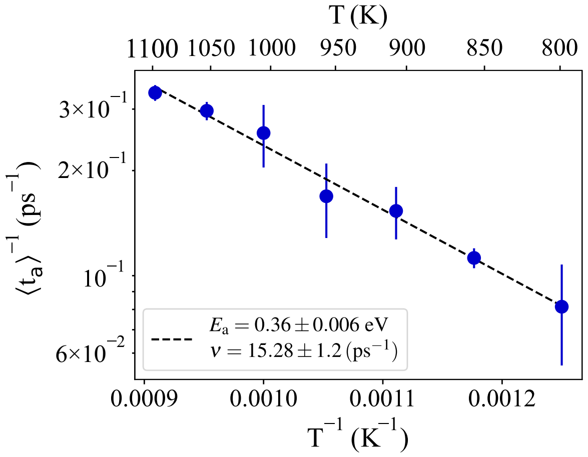

FIG. 7. The Arrhenius plot, through which the attempt frequency and activation energy for the recombination of the 3I+V defect cluster is calculated. At each temperature seven annealing MD simulations with the mod-GAP potential have been carried out. Uncertainties are standard error of the mean. With the estimated ν and E_a values, the average life time of the cluster at room temperature is predicted to be 0.0725 μs.

However, the formation energy of the final collapsed-into configuration in all cases is 5.30 eV. The average lifetime of the cluster $\langle t_\text{a} \rangle$ at different temperatures can be estimated using the Arrhenius equation as

$$\frac{1}{\langle t_\text{a} \rangle} = \nu \exp\left(\frac{-E_\text{a}}{k_\text{B} T}\right) \tag{6}$$

where E_a is the activation energy of recombination; ν is the attempt frequency; k_B is the Boltzmann constant, and T is the temperature. The attempt frequency and activation energy can be calculated by fitting Eq. (6) to the obtained recombination times at different simulated temperatures in an Arrhenius plot. Fig. 7 represents the fit and corresponding activation energy and attempt frequency for recombination of the cluster. The physics considerations for the Arrhenius fit presented in Fig. 6 are as follows. In order to have the transition state theory valid, the recombination time should not be shorter than about three lattice vibrations, or 1 ps. Otherwise, the recombination occurs in a time span that is shorter than the thermodynamic relaxation time, which breaks the transition state theory. Hence, we considered only the temperature range up to T_{max}, which was defined as the temperature at which the cluster did not recombine for at least 2–3 ps. T_{max} was found to be 1100 K. Starting from T_{max}, subsequent annealing simulations at temperatures down to the 800 K, with the narrower interval of 50 K were carried out. For each temperature seven cases were simulated. The average recombination time and the associated standard error of the mean at each temperature were considered in the fitting. Using the acquired attempt frequency of $\nu = 15.28$ ps^{-1} and activation energy of $E_\text{a} = 0.36$ eV, Eq. (6) predicts the life time of the cluster to be 0.0725 μs at room temperature.

V. CONCLUSION

We exploit the near-DFT accuracy of a Gaussian approximation machine-learning potential, GAP, to provide an *ab initio* perspective of the primary radiation damage in silicon. We show that there are perceptible differences between the predictions of GAP and traditional potentials in both the heat spike phase and in the final state of the defects. Regarding the threshold displacement energy, SW has the highest global average, where T3 and GAP potentials yield very close global average values. Moreover, in contrary to GAP, the global minimum threshold is found in low-index directions in classical potentials. Ion-beam mixing is greater in GAP by a factor a two. As for the final state of the damage, larger defect clusters have lower fraction in the simulations with GAP and survived defects are majorly in the form of small-sized clusters or isolated defects. We show that this feature arises from the form by which the cascades are evolving in GAP; a more-spread form of propagation compared to the confined-in-pocket form with classical potentials. We also present detailed assessment of the new defect cluster that we encountered in our previous work. This cluster is comprised of four defects where a vacancy is surrounded by three dumbbell interstitials, and its occurrence is higher in simulations with GAP. The cluster remains stable when quenched to 0 K and shows no recombination up to 700 K. The stability of the cluster comes from the four-folded bonding nature of the all atoms around the vacant position. The formation energy of this cluster is 5.97 eV by GAP compared to the 5.57 eV obtained with DFT calculations. Assuming that the Arrhenius equation holds for thermally-activated recombination of the cluster, $0.0725\,\mu$s was estimated as the average lifetime of the cluster at room temperature.

ACKNOWLEDGMENTS

Grants of computer capacity and resources from CSC-IT Center for Science, Finland, and from the center for high performance computing at Shahid Beheshti University, Iran, are gratefully acknowledged.

---

[1] J. A. Brinkman, On the nature of radiation damage in metals, J. Appl. Phys. **25**, 961 (1954).

[2] J. Lindhard, M. Scharff, and H. E. Schiøtt, *Range Concepts and Heavy Ion Ranges* (Munksgaard, Copenhagen, 1963).

[3] M. T. Robinson and I. M. Torrens, Computer simulation of atomic-displacement cascades in solids in the binary-collision approximation, Phys. Rev. B **9**, 5008 (1974).

[4] M. O. Ruault, J. Chaumont, J. M. Penisson, and A. Bourret, High resolution and in situ investigation of defects in bi-irradiated Si, Philos. Mag. A **50**, 667 (1984).

[5] J. Williams, Ion implantation of semiconductors, Mater. Sci. Eng. A **253**, 8 (1998).

[6] P. Sioshansi, Surface modification of industrial components by ion implantation, Mater. Sci. Eng. **90**, 373 (1987).

[7] K. Nordlund, S. J. Zinkle, A. E. Sand, F. Granberg, R. S. Averback, R. E. Stoller, T. Suzudo, L. Malerba, F. Banhart, W. J. Weber *et al.*, Primary radiation damage: A review of current understanding and models, J. Nucl. Mater. **512**, 450 (2018).

[8] A. E. Sand, D. R. Mason, A. D. Backer, X. Yi, S. L. Dudarev, and K. Nordlund, Cascade fragmentation: Deviation from power law in primary radiation damage, Mater. Res. Lett. **5**, 357 (2017).

[9] F. Djurabekova and K. Nordlund, Molecular dynamics simulations of non-equilibrium systems, in *Handbook of Materials Modeling: Applications: Current and Emerging Materials*, edited by W. Andreoni and S. Yip (Springer International Publishing, Cham, 2018), pp. 2161–2192.

[10] K. Nordlund and M. P. Short, Modeling of radiation damage in materials: Best practices and future directions, in *Handbook of Materials Modeling: Applications: Current and Emerging Materials*, edited by W. Andreoni and S. Yip (Springer International Publishing, Cham, 2018), pp. 2367–2379.

[11] K. Nordlund, Historical review of computer simulation of radiation effects in materials, J. Nucl. Mater. **520**, 273 (2019).

[12] A. E. Sand, M. J. Aliaga, M. J. Caturla, and K. Nordlund, Surface effects and statistical laws of defects in primary radiation damage: Tungsten vs. iron, Europhys. Lett. **115**, 36001 (2016).

[13] P. D. Lane, G. J. Galloway, R. J. Cole, M. Caffio, R. Schaub, and G. J. Ackland, Validating molecular dynamics with direct imaging of radiation damage debris, Phys. Rev. B **85**, 094111 (2012).

[14] R. Stoller, Primary radiation damage formation, in *Comprehensive Nuclear Materials*, edited by R. J. Konings (Elsevier, Oxford, 2012), pp. 293–332.

[15] M. W. Finnis and J. E. Sinclair, A simple empirical *N*-body potential for transition metals, Philos. Mag. A **50**, 45 (1984).

[16] M. I. Baskes, Application of the Embedded-Atom Method to Covalent Materials: A Semiempirical Potential for Silicon, Phys. Rev. Lett. **59**, 2666 (1987).

[17] J. Tersoff, Modeling solid-state chemistry: Interatomic potentials for multicomponent systems, Phys. Rev. B **39**, 5566 (1989).

[18] F. H. Stillinger and T. A. Weber, Computer simulation of local order in condensed phases of silicon, Phys. Rev. B **31**, 5262 (1985).

[19] A. C. T. van Duin, S. Dasgupta, F. Lorant, and W. A. Goddard, Reaxff: A reactive force field for hydrocarbons, J. Phys. Chem. A **105**, 9396 (2001).

[20] A. P. Bartók, M. C. Payne, R. Kondor, and G. Csányi, Gaussian Approximation Potentials: The Accuracy of Quantum Mechanics, without the Electrons, Phys. Rev. Lett. **104**, 136403 (2010).

[21] J. Behler and M. Parrinello, Generalized Neural-Network Representation of High-Dimensional Potential-Energy Surfaces, Phys. Rev. Lett. **98**, 146401 (2007).

[22] Y. Mishin, Machine-learning interatomic potentials for materials science, Acta Mater. **214**, 116980 (2021).

[23] A. P. Bartók, R. Kondor, and G. Csányi, On representing chemical environments, Phys. Rev. B **87**, 184115 (2013).

[24] R. Batra, H. D. Tran, C. Kim, J. Chapman, L. Chen, A. Chandrasekaran, and R. Ramprasad, General atomic neighbor-

hood fingerprint for machine learning-based methods, J. Phys. Chem. C **123**, 15859 (2019).
[25] M. J. Willatt, F. Musil, and M. Ceriotti, Atom-density representations for machine learning, J. Chem. Phys. **150**, 154110 (2019).
[26] R. Drautz, Atomic cluster expansion for accurate and transferable interatomic potentials, Phys. Rev. B **99**, 014104 (2019).
[27] N. Artrith, T. Morawietz, and J. Behler, High-dimensional neural-network potentials for multicomponent systems: Applications to zinc oxide, Phys. Rev. B **83**, 153101 (2011).
[28] N. Artrith, A. Urban, and G. Ceder, Efficient and accurate machine-learning interpolation of atomic energies in compositions with many species, Phys. Rev. B **96**, 014112 (2017).
[29] Y. Zuo, C. Chen, X. Li, Z. Deng, Y. Chen, J. Behler, G. Csányi, A. V. Shapeev, A. P. Thompson, M. A. Wood, and S. P. Ong, Performance and cost assessment of machine learning interatomic potentials, J. Phys. Chem. A **124**, 731 (2020).
[30] M. A. Caro, V. L. Deringer, J. Koskinen, T. Laurila, and G. Csányi, Growth Mechanism and Origin of High sp^3 Content in Tetrahedral Amorphous Carbon, Phys. Rev. Lett. **120**, 166101 (2018).
[31] M. A. Caro, G. Csányi, T. Laurila, and V. L. Deringer, Machine learning driven simulated deposition of carbon films: From low-density to diamondlike amorphous carbon, Phys. Rev. B **102**, 174201 (2020).
[32] Y.-X. Zhou, H.-Y. Zhang, V. L. Deringer, and W. Zhang, Structure and dynamics of supercooled liquid $Ge_2Sb_2Te_5$ from machine-learning-driven simulations, Phys. Status Solidi (RRL) **15**, 2000403 (2021).
[33] N. Artrith and A. M. Kolpak, Understanding the composition and activity of electrocatalytic nanoalloys in aqueous solvents: A combination of DFT and accurate neural network potentials, Nano Lett. **14**, 2670 (2014).
[34] V. L. Deringer, N. Bernstein, A. P. Bartók, M. J. Cliffe, R. N. Kerber, L. E. Marbella, C. P. Grey, S. R. Elliott, and G. Csányi, Realistic atomistic structure of amorphous silicon from machine-learning-driven molecular dynamics, J. Phys. Chem. Lett. **9**, 2879 (2018).
[35] V. L. Deringer, N. Bernstein, G. Csányi, C. Ben Mahmoud, M. Ceriotti, M. Wilson, D. A. Drabold, and S. R. Elliott, Origins of structural and electronic transitions in disordered silicon, Nature (London) **589**, 59 (2021).
[36] C. W. Rosenbrock, K. Gubaev, A. V. Shapeev, L. B. Pártay, N. Bernstein, G. Csányi, and G. L. W. Hart, Machine-learned interatomic potentials for alloys and alloy phase diagrams, npj Comput. Mater. **7**, 24 (2021).
[37] G. Sivaraman, A. N. Krishnamoorthy, M. Baur, C. Holm, M. Stan, G. Csányi, C. Benmore, and Á. Vázquez-Mayagoitia, Machine-learned interatomic potentials by active learning: Amorphous and liquid hafnium dioxide, npj Comput. Mater. **6**, 104 (2020).
[38] H. Wang, X. Guo, L. Zhang, H. Wang, and J. Xue, Deep learning inter-atomic potential model for accurate irradiation damage simulations, Appl. Phys. Lett. **114**, 244101 (2019).
[39] T. Wen, C.-Z. Wang, M. J. Kramer, Y. Sun, B. Ye, H. Wang, X. Liu, C. Zhang, F. Zhang, K.-M. Ho, and N. Wang, Development of a deep machine learning interatomic potential for metalloid-containing Pd-Si compounds, Phys. Rev. B **100**, 174101 (2019).
[40] H. Mirhosseini, H. Tahmasbi, S. R. Kuchana, S. A. Ghasemi, and T. D. Kühne, An automated approach for developing neural network interatomic potentials with flame, Comput. Mater. Sci. **197**, 110567 (2021).
[41] G. Nikoulis, J. Byggmästar, J. Kioseoglou, K. Nordlund, and F. Djurabekova, Machine-learning interatomic potential for W-Mo alloys, J. Phys.: Condens. Matter **33**, 315403 (2021).
[42] F. J. Domínguez-Gutiérrez, J. Byggmästar, K. Nordlund, F. Djurabekova, and U. von Toussaint, Computational study of crystal defect formation in Mo by a machine learning molecular dynamics potential, Modell. Simul. Mater. Sci. Eng. **29**, 055001 (2021).
[43] M. Babaei, Y. T. Azar, and A. Sadeghi, Locality meets machine learning: Excited and ground-state energy surfaces of large systems at the cost of small ones, Phys. Rev. B **101**, 115132 (2020).
[44] T. Morawietz and N. Artrith, Machine learning-accelerated quantum mechanics-based atomistic simulations for industrial applications, J. Comput.-Aided Mol. Des. **35**, 557 (2021).
[45] T. Kumagai, S. Izumi, S. Hara, and S. Sakai, Development of bond-order potentials that can reproduce the elastic constants and melting point of silicon for classical molecular dynamics simulation, Comput. Mater. Sci. **39**, 457 (2007).
[46] B.-J. Lee, A modified embedded atom method interatomic potential for silicon, Calphad **31**, 95 (2007).
[47] J. a. F. Justo, M. Z. Bazant, E. Kaxiras, V. V. Bulatov, and S. Yip, Interatomic potential for silicon defects and disordered phases, Phys. Rev. B **58**, 2539 (1998).
[48] J. Tersoff, New empirical approach for the structure and energy of covalent systems, Phys. Rev. B **37**, 6991 (1988).
[49] A. P. Bartók, J. Kermode, N. Bernstein, and G. Csányi, Machine Learning a General-Purpose Interatomic Potential for Silicon, Phys. Rev. X **8**, 041048 (2018).
[50] Y. Wang, J. Ding, Z. Fan, L. Tian, M. Li, H. Lu, Y. Zhang, E. Ma, J. Li, and Z. Shan, Tension–compression asymmetry in amorphous silicon, Nat. Mater. **20**, 1371 (2021).
[51] A. Hamedani, J. Byggmästar, F. Djurabekova, G. Alahyarizadeh, R. Ghaderi, A. Minuchehr, and K. Nordlund, Insights into the primary radiation damage of silicon by a machine learning interatomic potential, Mater. Res. Lett. **8**, 364 (2020).
[52] K. Nordlund, N. Runeberg, and D. Sundholm, Repulsive interatomic potentials calculated using Hartree-Fock and density-functional theory methods, Nucl. Instrum. Methods Phys. Res., Sect. B **132**, 45 (1997).
[53] A. Zinoviev and K. Nordlund, Comparison of repulsive interatomic potentials calculated with an all-electron DFT approach with experimental data, Nucl. Instrum. Methods Phys. Res., Sect. B **406**, 511 (2017).
[54] G. Kresse and J. Hafner, *Ab initio* molecular dynamics for liquid metals, Phys. Rev. B **47**, 558 (1993).
[55] G. Kresse and J. Hafner, *Ab initio* molecular-dynamics simulation of the liquid-metal–amorphous-semiconductor transition in germanium, Phys. Rev. B **49**, 14251 (1994).
[56] G. Kresse and J. Furthmüller, Efficiency of ab-initio total energy calculations for metals and semiconductors using a plane-wave basis set, Comput. Mater. Sci. **6**, 15 (1996).
[57] G. Kresse and J. Furthmüller, Efficient iterative schemes for *ab initio* total-energy calculations using a plane-wave basis set, Phys. Rev. B **54**, 11169 (1996).

[58] J. P. Perdew, K. Burke, and M. Ernzerhof, Generalized Gradient Approximation Made Simple, Phys. Rev. Lett. **77**, 3865 (1996).

[59] P. E. Blöchl, Projector augmented-wave method, Phys. Rev. B **50**, 17953 (1994).

[60] G. Kresse and D. Joubert, From ultrasoft pseudopotentials to the projector augmented-wave method, Phys. Rev. B **59**, 1758 (1999).

[61] P. Olsson, C. S. Becquart, and C. Domain, *Ab initio* threshold displacement energies in iron, Mater. Res. Lett. **4**, 219 (2016).

[62] J. Byggmästar, F. Granberg, and K. Nordlund, Effects of the short-range repulsive potential on cascade damage in iron, J. Nucl. Mater. **508**, 530 (2018).

[63] J. Byggmästar, A. Hamedani, K. Nordlund, and F. Djurabekova, Machine-learning interatomic potential for radiation damage and defects in tungsten, Phys. Rev. B **100**, 144105 (2019).

[64] K. Nordlund, J. Wallenius, and L. Malerba, Molecular dynamics simulations of threshold displacement energies in Fe, Nucl. Instrum. Methods Phys. Res., Sect. B **246**, 322 (2006).

[65] A. Chakrabory and P. Eisenlohr, Consistent visualization and uniform sampling of crystallographic directions, Technical Report, Michigan State University, 2017.

[66] J. Byggmästar, K. Nordlund, and F. Djurabekova, Gaussian approximation potentials for body-centered-cubic transition metals, Phys. Rev. Materials **4**, 093802 (2020).

[67] S. J. Clark and G. J. Ackland, *Ab initio* calculations of the self-interstitial in silicon, Phys. Rev. B **56**, 47 (1997).

[68] S. Plimpton, Fast parallel algorithms for short-range molecular dynamics, J. Comput. Phys. **117**, 1 (1995).

[69] [https://lammps.sandia.gov/index.html].

[70] QUIP - QUantum mechanics and Interatomic Po-tentials [https://github.com/libAtoms/QUIP].

[71] T. Schneider and E. Stoll, Molecular-dynamics study of a three-dimensional one-component model for distortive phase transitions, Phys. Rev. B **17**, 1302 (1975).

[72] J. F. Ziegler, U. Littmark, and J. P. Biersack, *The Stopping and Range of Ions in Solids* (Pergamon, New York, 1985).

[73] K. Nordlund, Molecular dynamics simulation of ion ranges in the 1–100 keV energy range, Comput. Mater Sci. **3**, 448 (1995).

[74] J. F. Ziegler, SRIM-2013 software package, www.srim.org.

[75] A. Stukowski, Visualization and analysis of atomistic simulation data with OVITO–the open visualization tool, Modell. Simul. Mater. Sci. Eng. **18**, 015012 (2009).

[76] K. Nordlund, M. Ghaly, and R. S. Averback, Mechanisms of ion beam mixing in metals and semiconductors, J. Appl. Phys. **83**, 1238 (1998).

[77] K. Nordlund and R. S. Averback, Atomic displacement processes in irradiated amorphous and crystalline silicon, Appl. Phys. Lett. **70**, 3101 (1997).

[78] C. J. Ortiz, P. Pichler, T. Fühner, F. Cristiano, B. Colombeau, N. E. B. Cowern, and A. Claverie, A physically based model for the spatial and temporal evolution of self-interstitial agglomerates in ion-implanted silicon, J. Appl. Phys. **96**, 4866 (2004).

[79] K. Nordlund, M. Ghaly, R. S. Averback, M. Caturla, T. Diaz de la Rubia, and J. Tarus, Defect production in collision cascades in elemental semiconductors and fcc metals, Phys. Rev. B **57**, 7556 (1998).

[80] R. Radu, I. Pintilie, L. F. Makarenko, E. Fretwurst, and G. Lindstroem, Kinetics of cluster-related defects in silicon sensors irradiated with monoenergetic electrons, J. Appl. Phys. **123**, 161402 (2018).

[81] M. Aboy, I. Santos, L. Pelaz, L. A. Marqués, and P. López, Modeling of defects, dopant diffusion and clustering in silicon, J. Comput. Electron. **13**, 40 (2014).

[82] S. A. Fischer, C. M. Isborn, and O. V. Prezhdo, Excited states and optical absorption of small semiconducting clusters: Dopants, defects and charging, Chem. Sci. **2**, 400 (2011).

[83] R. M. Fleming, C. H. Seager, E. Bielejec, G. Vizkelethy, D. V. Lang, and J. M. Campbell, Defect annealing in neutron and ion damaged silicon: Influence of defect clusters and doping, J. Appl. Phys. **107**, 053712 (2010).

[84] S. Koelling, O. Richard, H. Bender, M. Uematsu, A. Schulze, G. Zschaetzsch, M. Gilbert, and W. Vandervorst, Direct imaging of 3d atomic-scale dopant-defect clustering processes in ion-implanted silicon, Nano Lett. **13**, 2458 (2013).

[85] A. Chroneos, R. W. Grimes, and H. Bracht, Impact of germanium on vacancy clustering in germanium-doped silicon, J. Appl. Phys. **105**, 016102 (2009).

[86] R. Radu, I. Pintilie, L. C. Nistor, E. Fretwurst, G. Lindstroem, and L. F. Makarenko, Investigation of point and extended defects in electron irradiated silicon-dependence on the particle energy, J. Appl. Phys. **117**, 164503 (2015).

[87] A. Chroneos, C. A. Londos, E. N. Sgourou, and P. Pochet, Point defect engineering strategies to suppress A-center formation in silicon, Appl. Phys. Lett. **99**, 241901 (2011).

[88] S. Lee and G. S. Hwang, Structure and stability of small compact self-interstitial clusters in crystalline silicon, Phys. Rev. B **77**, 085210 (2008).

[89] D. A. Richie, J. Kim, S. A. Barr, K. R. A. Hazzard, R. Hennig, and J. W. Wilkins, Complexity of Small Silicon Self-Interstitial Defects, Phys. Rev. Lett. **92**, 045501 (2004).